Degenerate Interpretations of O₃ Spectral Features in Exoplanet Atmosphere Observations Due to Stellar UV Uncertainties: A 3D Case Study with TRAPPIST-1 e

G. J. Cooke[1,2] , D. R. Marsh[1] , C. Walsh[1] , and A. Youngblood[3]
[1] School of Physics and Astronomy, University of Leeds, Leeds LS2 9JT, UK; gjc53@cam.ac.uk
[2] Institute of Astronomy, University of Cambridge, UK
[3] NASA Goddard Space Flight Center, Solar System Exploration Division, 8800 Greenbelt Road, Greenbelt, MD 20771, USA

Abstract

TRAPPIST-1 e is a potentially habitable terrestrial exoplanet orbiting an ultracool M dwarf star and is a key target for observations with the James Webb Space Telescope. One-dimensional photochemical modeling of terrestrial planetary atmospheres has shown the importance of the incoming stellar UV flux in modulating the concentration of chemical species, such as O_3 and H_2O. In addition, three-dimensional (3D) modeling has demonstrated anisotropy in chemical abundances due to transport in tidally locked exoplanet simulations. We use the Whole Atmosphere Community Climate Model Version 6 (WACCM6), a 3D Earth system model, to investigate how uncertainties in the incident UV flux, combined with transport, affect observational predictions for TRAPPIST-1 e (assuming an initial Earth-like atmospheric composition). We use two semiempirical stellar spectra for TRAPPIST-1 from the literature. The UV flux ratio between them can be as large as a factor of 5000 in some wavelength bins. Consequently, the photochemically produced total O_3 columns differ by a factor of 26. Spectral features of O_3 in both transmission and emission spectra vary between these simulations (e.g., differences of 20 km in the transmission spectrum effective altitude for O_3 at 0.6 μm). This leads to potential ambiguities when interpreting observations, including overlap with scenarios that assume alternative O_2 concentrations. Hence, to achieve robust interpretations of terrestrial exoplanetary spectra, characterization of the UV spectra of their host stars is critical. In the absence of such stellar measurements, atmospheric context can still be gained from other spectral features (e.g., H_2O), or by comparing direct imaging and transmission spectra in conjunction.

Unified Astronomy Thesaurus concepts: Exoplanet atmospheres (487); Exoplanets (498); Exoplanet atmospheric composition (2021); Transmission spectroscopy (2133)

1. Introduction

On account of their frequency and relative ease of characterization, planetary systems orbiting M dwarf stars are prime targets in the search for potentially habitable exoplanets. TRAPPIST-1 is an M8.5V star, orbited by seven terrestrial exoplanets, and each of them could be tidally locked to their host star (Gillon et al. 2017). TRAPPIST-1 e is of particular interest because with current knowledge it is more likely than the close-in planets to have retained its atmosphere due to lower predicted escape rates (Dong et al. 2018), and is probably more able to sustain surface liquid water when compared to the outer planets which receive less stellar irradiation (Gillon et al. 2017; Wolf 2017). To begin to characterize the TRAPPIST-1 exoplanets and determine the compositions of their atmospheres, at the time of writing, several observational programs with the James Webb Space Telescope (JWST) are scheduled, including the observation of four transits of TRAPPIST-1 e in 2023 (see program 1331).[4]

In general, the detection of molecular oxygen (O_2) on an exoplanet is of profound interest because of its importance for life on Earth (Segura et al. 2003; Meadows et al. 2018). Ozone (O_3) is produced in exoplanetary atmospheres by UV radiation

which is able to dissociate O_2, and it has been calculated that in some situations the detection of O_3 is easier to achieve than a detection of O_2; for example, for low O_2 concentrations like those potentially present during Earth's Proterozoic Eon, but where O_3 concentrations are still detectable (Kozakis et al. 2022). Thus, in such cases, it has been proposed that the detection of O_3 may be used as a proxy to confirm the presence of O_2 (Leger et al. 1993; Segura et al. 2003; Meadows et al. 2018; Quanz et al. 2021).

One-dimensional (1D) photochemical modeling has demonstrated that planetary atmospheric composition (including O_3 and H_2O) is influenced by the strength and shape of the incoming UV radiation from the host star (see Rugheimer et al. 2013; Grenfell et al. 2014; Meadows et al. 2018; Kozakis et al. 2022, and references therein). For example, Teal et al. (2022) used MUSCLES Treasury Survey M dwarf spectra combined with UV spectra reconstructions as stellar spectra input to Atmos (a coupled 1D photochemistry and climate model), and similarly demonstrated that UV irradiation can modulate hydrocarbon haze concentrations. Because the atmospheric composition with respect to altitude affects molecular detectability in remote sensing, the link between O_3 abundance and O_2 abundance will be difficult to ascertain because it depends on several parameters, including the catalytic cycles that remove O_3 (e.g., the HO_x, NO_x, ClO_x, and BrO_x chemical families), and atmospheric pressure. A well-characterized spectrum of the host star is required for confident modeling of planetary climate (Eager-Nash et al. 2020), atmospheric chemistry (Kozakis et al. 2022), and atmospheric escape (Dong et al. 2018). However, the host star's spectral energy

---

[4] https://www.stsci.edu/jwst/science-execution/program-information.html?id=1331, accessed 2023 April 12.

distribution may not be known to high precision when analyzing and interpreting exoplanet observations.

The UV flux from TRAPPIST-1 remains uncertain because of the intrinsic faintness of the star ($V = 18.798$ mag; Costa et al. 2006). Peacock et al. (2019; henceforth P19) modeled the spectrum of TRAPPIST-1. To do this, they used the PHOENIX stellar atmospheric code (Hauschildt 1993; Hauschildt & Baron 2006; Baron & Hauschildt 2007), and added a treatment of the chromosphere to produce synthetic stellar spectra of cool dwarf stars, including TRAPPIST-1, whose UV light has a negligible flux contribution from the photosphere. More recently, Wilson et al. (2021b; hereafter W21) used new observations of TRAPPIST-1 to create a semiempirical spectrum for use in atmospheric modeling simulations. While neither spectrum wholly represents the true stellar irradiation environment of the TRAPPIST-1 planets, the W21 spectrum is in significantly better agreement with available observations of TRAPPIST-1.

In addition to the incoming stellar spectrum, the three-dimensional (3D) transport and chemistry of the exoplanet's atmosphere is important for understanding the distribution and abundance of chemical species. Chen et al. (2019) investigated exoplanets orbiting at the inner edge of the habitable zone using a 3D chemistry climate model (WACCM4), showing how different assumed UV spectra can influence atmospheric mixing ratios of species such as H_2O, O_3, and H. Additionally, 3D simulation studies have demonstrated the influence of UV radiation on 3D transport (Chen et al. 2019), stratospheric temperature (Godolt et al. 2015; Chen et al. 2019), and the distribution and abundance of chemical species (Chen et al. 2018, 2019, 2021; Braam et al. 2022; Ridgway et al. 2023). Tidally locked terrestrial exoplanets modeled in 3D exhibit atmospheric jets that transport heat and chemical constituents to the nightside (Showman & Polvani 2011; Eager-Nash et al. 2020; Yates et al. 2020). Proedrou & Hocke (2016), Chen et al. (2018), and Yates et al. (2020) found that O_3, which is photochemically generated on the dayside, can be transported to the nightside, where its lifetime increases due to the lack of UV irradiation and a reduction in catalytic cycle destruction. This body of previous work motivates the need to use 3D models when investigating the climate and chemistry of specific exoplanets, in particular, with respect to their molecular observability linked to the oxygenation state of the atmosphere.

In this study we simulate the atmosphere of TRAPPIST-1 e using the WACCM6 Earth system model and the stellar spectra from P19 (Peacock 2020, model 1A, version 1) and W21 (Wilson et al. 2021a, version 7), which differ in UV flux in some wavelength bins by up to a factor of 5000. Our aim is to quantify the effects of such uncertainties in the strength of UV from the host star on the climate and composition of the atmosphere. This is the first time a 3D global climate model has been used to assess the influence of uncertain UV spectra and transport on the climate and chemistry of TRAPPIST-1 e simultaneously. Additionally, we simulate possible future observations (transmission and emission spectra) of TRAP-PIST-1 e using the outputs from the WACCM6 simulations. We discuss the implications of uncertainties in the stellar UV spectrum in the interpretation of future observations of terrestrial exoplanets.

2. Methods

2.1. UV Spectra Input

This work employs two different assumed stellar spectra as input to the simulations. P19 generated three different models of TRAPPIST-1's spectrum (Models 1A, 2A, and 2B). Model 1A was created such that the emission was benchmarked to the Lyα reconstruction that was presented in Bourrier et al. (2017), who used the Hubble Space Telescope (HST) Space Telescope Imaging Spectrograph instrument to observe the TRAPPIST-1 Lyα line. Using an alternative approach to construct Model 2A and Model 2B, P19 aligned the stellar emission to be within the range of distance-corrected Galaxy Evolution Explorer near-ultraviolet photometry of stars with a spectral type akin to TRAPPIST-1, while remaining compatible with far-ultraviolet upper limits. The extreme-ultraviolet (EUV) estimates were extracted from empirical scaling relationships based on X-ray and Lyα emission.

W21 used new HST (1100–5500 Å) and XMM-Newton (10–50 Å) observations of TRAPPIST-1 from the Measure-ments of the Ultraviolet Spectral Characteristics of Low-Mass Exoplanetary Systems (Mega-MUSCLES) Treasury Survey (Froning et al. 2019; W21) to construct a 5 Å to 100 μm spectrum of the star. Four models were used to fill in gaps in wavelength coverage, including a PHOENIX model for wavelengths >5500 Å (>0.55 μm). Because of TRAPPIST-1's relatively low luminosity, W21 substituted the noisy 1100–4200 Å HST spectrum with a semiempirical, noiseless spectrum that reproduced the measured flux of detected UV emission lines and agreed with the upper limits on the stellar continuum established by the HST spectra.

W21 found that while the P19 Model 1A shows good agreement with the C II and Ca II stellar lines, several other lines are inconsistent with the measured fluxes, exhibiting a discrepancy $\sim$10 times more than the W21 upper limits permit. In the WACCM6 simulations, we decided to use both the P19 and W21 spectra in order to illustrate important differences that may occur in instances where the exoplanet's photochemical environment is highly uncertain.

2.2. WACCM6

TRAPPIST-1 is an ultracool M dwarf at a distance of 12.4 pc. Its stellar properties are summarized in Table 1. We assume that TRAPPIST-1 e receives 900 W m^{-2} of irradiation (0.66 $S_\oplus$, where $S_\oplus$ is the total insolation received by the Earth). This is consistent with the value used in the TRAPPIST-1 Habitable Atmosphere Intercomparison project (THAI; Fauchez et al. 2020a; Turbet et al. 2022), although note that the latest data available in the NASA Exoplanet Archive (Akeson et al. 2013) list a value of 0.646 ± 0.025 $S_\oplus$ (Agol et al. 2021).

We use the Earth system model WACCM6 to simulate the climate of TRAPPIST-1 e with the properties indicated in Table 1, using given values from from Delrez et al. (2018) and Grimm et al. (2018). Note that the simulations were started in 2020, before Agol et al. (2021) published their work. WACCM6 is a specific configuration of the Community Earth System Model version 2 (CESM2). The model release we use in this work is CESM2.1.3.[5] We use a preindustrial atmosphere (approximating the atmosphere of 1850 in terms of pollutants

---
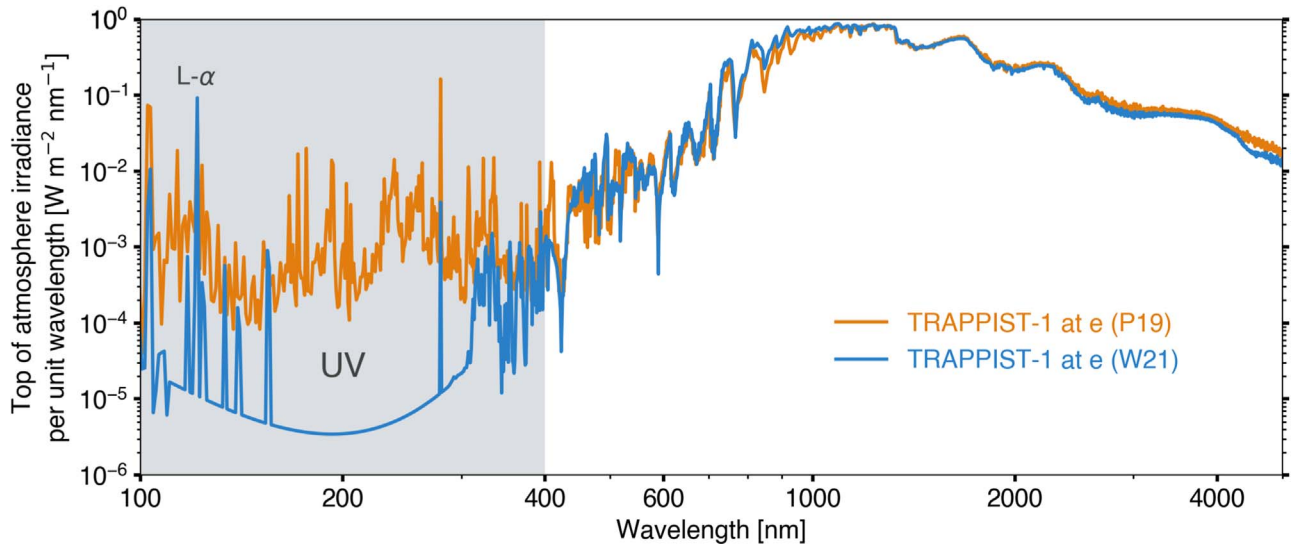
Figure 1. The top of atmosphere irradiance per unit wavelength as a function of wavelength for the TRAPPIST-1 semiempirical stellar spectra from P19 (orange) and W21 (light blue), each of which are scaled to the total integrated irradiance received by TRAPPIST-1 e (900 W m^{-2}). These spectra were rebinned in order to match the wavelength grid used in the WACCM6 simulations. The gray shaded region indicates UV wavelengths (100–400 nm).

and greenhouse gas mixing ratios) with the modern ocean and land configuration, a horizontal resolution of $1°.875$ by $2°.5$ (latitude by longitude), and 70 vertical atmospheric levels. The ocean and atmosphere are fully interactive, meaning that they respond to physical perturbations such as temperature, or in the case of the atmosphere, chemical perturbations. Because TRAPPIST-1 e is suspected to be tidally locked (Gillon et al. 2017), we lock the substellar point by fixing the solar zenith angle in each grid cell, and we set the exoplanet's obliquity and orbital eccentricity to zero (note that the eccentricity may be nonzero, albeit <0.01; Luger et al. 2017). The substellar point is placed in the Pacific Ocean at 180° longitude and 0° latitude. The chemical mechanism, which is described in Emmons et al. (2020), has 98 chemical species and 298 chemical reactions (including photochemical reactions). Absorption by CO_2 and H_2O in the Schumann–Runge bands is included (Ji et al. 2023). The full details of the model setup, alongside simulation scripts, are available via GitHub.[6]

We scale the P19 and W21 spectra to the irradiance received by TRAPPIST-1 e (900 W m^{-2}), rebinning them to match the wavelength grid required for the WACCM6 simulations. The resulting spectra are shown in Figure 1. For the wavelength regions over which O_2 and O_3 photolyse, the integrated flux is listed in Table 2.

We present 10 simulations with WACCM6, five with the P19 spectrum, and five with the W21 spectrum—see Table 3 for a summary. The initial conditions for the five simulations with each spectrum consist of one with the standard initial preindustrial Earth composition (PI), then three lower O_2 simulations with a composition with 10, 100, and 1000 times less O_2 (10% of the present atmospheric level (PAL) of O_2, 1% PAL, and 0.1% PAL, respectively), and one in which the planet is not tidally locked (noTL). These simulations allow us to assess the influence of different strengths of incoming UV spectra, the influence of tidal locking, and the effects of reducing O_2 in order to quantify any degeneracies between O_2, O_3, and incident UV light. Each simulation is run for over 250

Table 1
Orbital and Planetary Parameters Used in this Study, for the Exoplanet TRAPPIST-1 e and Its Star (TRAPPIST-1)

Parameter	Value
Stellar luminosity [$L_\odot$]	0.000553
Stellar effective temperature [K]	2566
Stellar radius [$R_\odot$]	0.119
Stellar mass [$M_\odot$]	0.089
Stellar metallicity	0.04
Planetary orbital period [days]	6.099
Planetary radius [$R_\oplus$]	0.91
Planetary mass [$M_\oplus$]	0.772
Planetary surface gravity [m s^{-2}]	9.14

Note. The parameters are from Delrez et al. (2018), Grimm et al. (2018), and Agol et al. (2021). The mass and radius are chosen to be consistent with the THAI project (Fauchez et al. 2020a; Sergeev et al. 2022a; Turbet et al. 2022). The $\odot$ and $\oplus$ subscripts denote values relative to the Sun and Earth, respectively.

model Earth years, and the last 10 years of the simulation are used for time-averaged results (Figures 2–6 and Figures 9–11). The WACCM6 simulations were run on 120 cores at a model cost of 1332 core-hours per simulated year. A 250 yr simulation therefore costs 333,000 core-hours.

2.3. Planetary Spectrum Generator

We use the Planetary Spectrum Generator (PSG; Villanueva et al. 2018) GlobES[7] 3D mapping tool to compute transmission and emission spectra from the WACCM6 atmospheric simulations, using instantaneous data (a "snapshot" at a model time step rather than an average over model time steps) for each produced spectrum. The WACCM6 instantaneous data are rebinned to a resolution of 10° in longitude only and we keep the same latitudinal grid resolution ($1°.875$). This is done to reduce the data size so it is compatible with GlobES in PSG, and is the same approach as used in Cooke et al. (2023). The

---

[6] https://github.com/exo-cesm/CESM2.1.3/tree/main/Tidally_locked exoplanets

[7] https://psg.gsfc.nasa.gov/apps/globes.php

Table 2
For the Two Different Spectra Used in the Simulations, the Integrated flux (in Units of W m^{-2}) is Given for Each Spectrum for the Total Flux and Six Different Wavelength Bands: Schumman–Runge Continuum (S-RC), Schumman–Runge Bands (S-RB), Herzberg Continuum (HC), Hartley Band (HaB), Huggins Band (HuB), and the Chappuis Band (CB)

Spectrum	Total 10.5–99,975 nm	S-RC 130–175 nm	S-RB 176–192 nm	HC 200–240 nm	HaB 200–310 nm	HuB 310–340 nm	CB 400–650 nm
Sun	1361	0.0092	0.0373	1.2997	19.8916	23.4556	453.7313
TP-1 P19	900	0.0382	0.0239	0.0841	0.3953	0.0829	2.1355
TP-1 W21	900	0.0025	0.0001	0.0002	0.0050	0.0133	2.3045
Flux ratio $\frac{P19}{W21}$	1.00	15.54	451.81	528.85	79.59	6.21	0.93

Note. For reference, the Earth receives 1360 W m^{-2} of irradiation. Photons in the S-RC, S-RB, and HC are able to photolyse O_2. Photons in the HaB, HuB, and CB, are able to photolyse O_3.

Table 3
Ten Simulations Have Been Performed, Each with an Obliquity of 0° and a Circular Orbit, Using Two Different Spectra for TRAPPIST-1 from P19 and W21 (See Text for the UV Spectra Input Details)

Simulation	Spectrum	O_2 mixing ratio [PAL]	Orbital parameters
P19 PI	P19	1	Tidally locked, 6.1 day rotational period
P19 10% PAL	P19	0.1	Tidally locked, 6.1 day rotational period
P19 1% PAL	P19	0.01	Tidally locked, 6.1 day rotational period
P19 0.1% PAL	P19	0.001	Tidally locked, 6.1 day rotational period
P19 noTL	P19	1	Not tidally locked, 1 day rotational period
W21 PI	W21	1	Tidally locked, 6.1 day rotational period
W21 10% PAL	W21	0.1	Tidally locked, 6.1 day rotational period
W21 1% PAL	W21	0.01	Tidally locked, 6.1 day rotational period
W21 0.1% PAL	W21	0.001	Tidally locked, 6.1 day rotational period
W21 noTL	W21	1	Not tidally locked, 1 day rotational period

Note. Eight simulations were set up in a tidally locked configuration with a 6.1 day rotation rate. The "PI" simulations have an initial preindustrial Earth composition and are the same apart from using the P19 and W21 spectra. The "noTL" simulations have an initial preindustrial Earth composition, are not tidally locked, and have a diurnal cycle (rotational period of 1 day). For the lower O_2 scenarios, the volume mixing ratio of atmospheric O_2 is reduced by a factor of 10, 100, and 1000 (the "10% PAL,""1% PAL," and "0.1% PAL" simulations, respectively). The PAL of oxygen is a volume mixing ratio of 0.21.

same data at the same time step are used for both transmission spectra and emission spectra in this paper. PSG ingests the data and integrates across the whole observable disk to produce a reflection or emission spectrum. It uses the grid cells at the terminator to produce a transmission spectrum. Because model grid cells either side of the terminator would contribute to the opacity of the atmosphere, this is not the most realistic way to represent the atmospheric geometry during a planetary transit (Caldas et al. 2019). However, it is adequate for the relatively low temperature contrasts between the dayside and nightside for the TRAPPIST-1 e atmospheres simulated here.
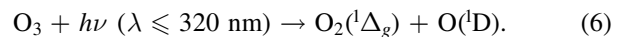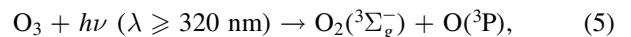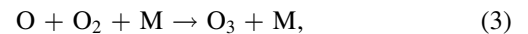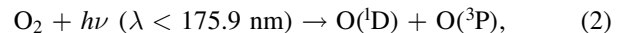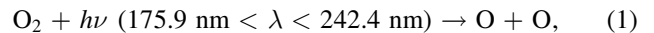
The molecules we use for the computation of the transmission and emission spectra are N_2, O_2, CO_2, H_2O, O_3, CH_4, and N_2O, which is a list that includes possible biosignatures and indicators of habitability (Kaltenegger 2017). The default HITRAN opacity data (Gordon et al. 2017) are used for each molecule, as well as all available collision-induced absorption coefficients (e.g., O_2–O_2, N_2–N_2, and O_2–N_2). The radiative transfer model used in PSG is the Planetary and Universal Model of Atmospheric Scattering (PUMAS) model. The correlated-k method is used by PUMAS for the spectral resolving powers used in this paper (Villanueva et al. 2018). If high resolution is required, it would instead use the line-by-line method. Scattering effects are included, as are ice clouds and water clouds. The effective radius of the cloud particles is assumed to be 5 μm for water and 100 μm for ice clouds. The data associated with this paper are openly available from the

University of Leeds Data Repository (doi:10.5518/1424). The figures, as well as PSG files, can be generated from this data.

3. Results

3.1. Atmospheric Chemistry

Atmospheric O_3 is created and destroyed via the Chapman cycle (Chapman 1930), which is initiated by UV light (of wavelength λ) dissociating an O_2 molecule:

$$O_2 + h\nu \ (175.9 \ nm < \lambda < 242.4 \ nm) \rightarrow O + O, \quad (1)$$

$$O_2 + h\nu \ (\lambda < 175.9 \ nm) \rightarrow O(^1D) + O(^3P), \quad (2)$$

$$O + O_2 + M \rightarrow O_3 + M, \quad (3)$$

$$O + O_3 \rightarrow 2O_2, \quad (4)$$

$$O_3 + h\nu \ (\lambda \geqslant 320 \ nm) \rightarrow O_2(^3\Sigma_g^-) + O(^3P), \quad (5)$$

$$O_3 + h\nu \ (\lambda \leqslant 320 \ nm) \rightarrow O_2(^1\Delta_g) + O(^1D). \quad (6)$$

The latter two photolysis reactions do not contribute to O_3 destruction because the O produced rapidly recombines with O_2 to produce O_3 via reaction (3). However, the reaction between O and O_3 (reaction 4) does lead to a loss of O_3, and it can be sped up through catalytic agents, which are denoted
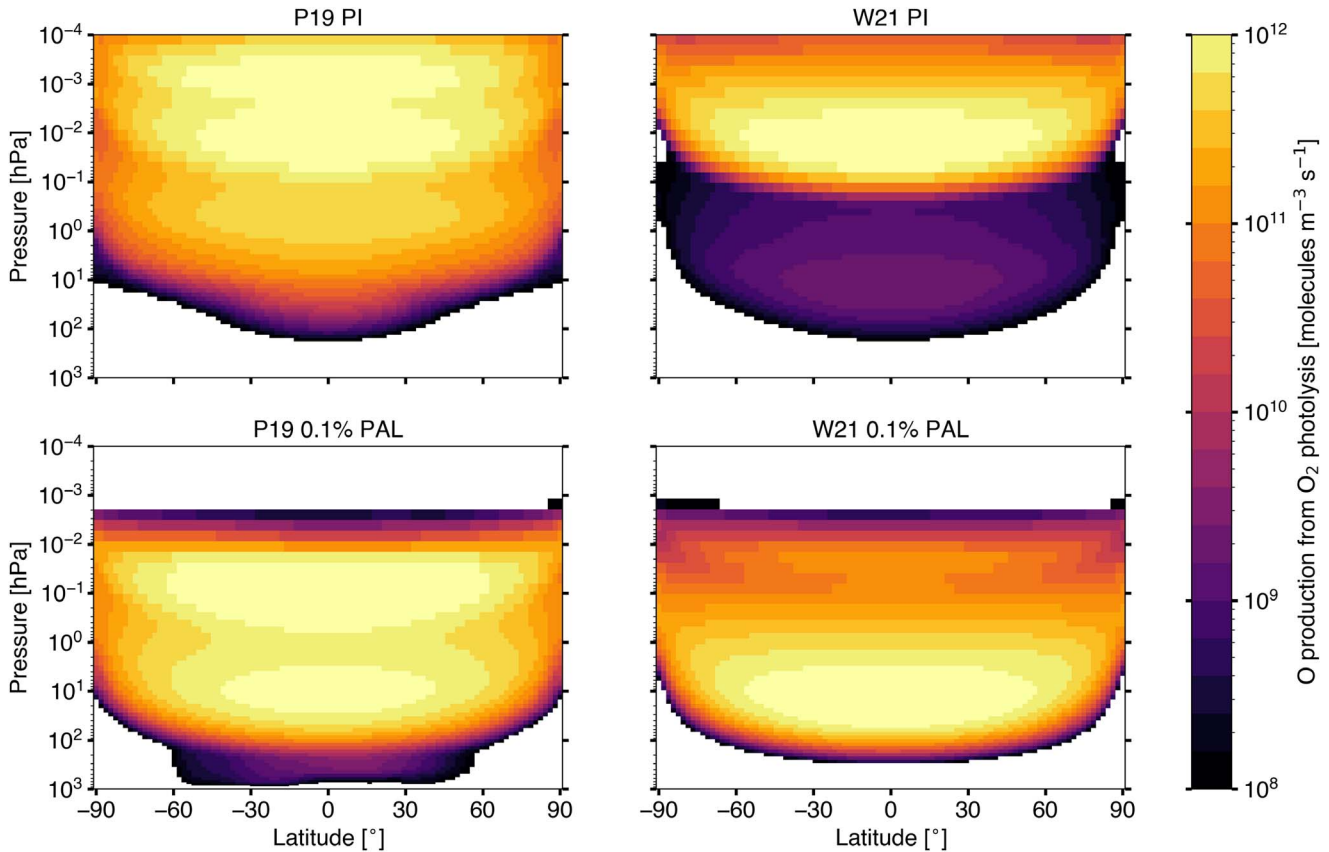
Figure 2. The P19 (left column) and W21 (right column) irradiation scenarios are compared to each other for the PI (top row) and 0.1% PAL (bottom row) cases. The zonal mean (averaged over longitude) of the production of O from O_2 photolysis is displayed, with latitude in degrees on the horizontal axis and pressure in hectopascals on the vertical axis. O_2 photolysis takes place at wavelengths less than 242 nm. The white regions show where the production has dropped below 10^8 molecules m^{-3} s^{-1}.

below as X. An example of a catalytic cycle is shown here:

$$X + O_3 \rightarrow XO + O_2,$$
$$XO + O \rightarrow X + O_2,$$
$$\text{Overall: } O_3 + O \rightarrow 2O_2. \tag{7}$$
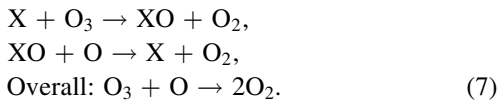
Catalytic agents may be NO, H, OH, Cl, or Br (Brasseur & Solomon 2005). These species can be produced through other photolysis reactions (e.g., H_2O photolysis producing H and OH).

Figure 2 shows the zonal mean of O production from O_2 photolysis in the P19 PI, P19 0.1% PAL, W21 PI, and W21 0.1% PAL simulations. In the two PI simulations, O_2 can be photolysed lower down in the P19 case because there is more incoming UV radiation than in the W21 case. When O_2 is reduced to 0.1% PAL, it can be seen that the peak of O_2 photolysis moves to higher pressures (downward in altitude). Where O is produced impacts the number density of O_3. Figure 3 shows the zonal mean of the O_3 number density for the same set of simulations as in Figure 2. Reducing O_2 in the P19 cases causes a drop in the O_3 number density at pressures above 1 hPa, while the opposite occurs in the W21 cases. This is because of the pressure dependency on the reaction that produces O_3 (reaction 3).

In Figure 4 we show the global mean vertical profiles for temperature, and the mixing ratios of O, O_2, O_3, H_2O, CH_4, N_2O, and CO_2. On global average, the temperature profile shows deviations of up to 9 K in the troposphere and up to

19 K below the thermosphere between the W21 PI and P19 PI simulations. The W21 PI middle atmosphere (between the troposphere and thermosphere) is colder than the P19 PI middle atmosphere due to reduced O_3 heating because of the lower O_3 concentration. The P19 noTL simulation has a lower temperature in the troposphere by up to 23 K and in the middle atmosphere by up to 6 K, resulting in lower concentrations of H_2O compared to the P19 PI simulation. Generally, between 200 and 10 hPa, the relative H_2O number density in each simulation correlates with the relative temperature profile in each simulation (i.e., a lower temperature results in less H_2O).

The O_3 mixing ratio profile in Figure 4 shows large deviations between the P19 PI (orange) and W21 PI (light blue) simulations, with a difference of a factor of 152 in the mixing ratio at the surface. The globally averaged O_3 number density peaks at 2.0×10^{19} molecules m^{-3} at 50 hPa in the P19 PI case and at 7.0×10^{17} molecules m^{-3} at 50 hPa in the W21 PI case. Despite the amount of O_3 present in the P19 PI simulated atmosphere, the temperature inversion in the middle atmosphere is <8 K because the UV intensity is not sufficient to provide enough O_3 UV heating to create a similar temperature inversion in Earth's stratosphere ($\approx$60 K change between the tropopause and stratopause). The P19 noTL simulation (dark red) shows that tidal locking increases the amount of O_3 in the middle atmosphere, while reducing the O_3 concentration in the troposphere. The non–tidally locked cases are colder in the lower atmosphere, and warmer in the middle
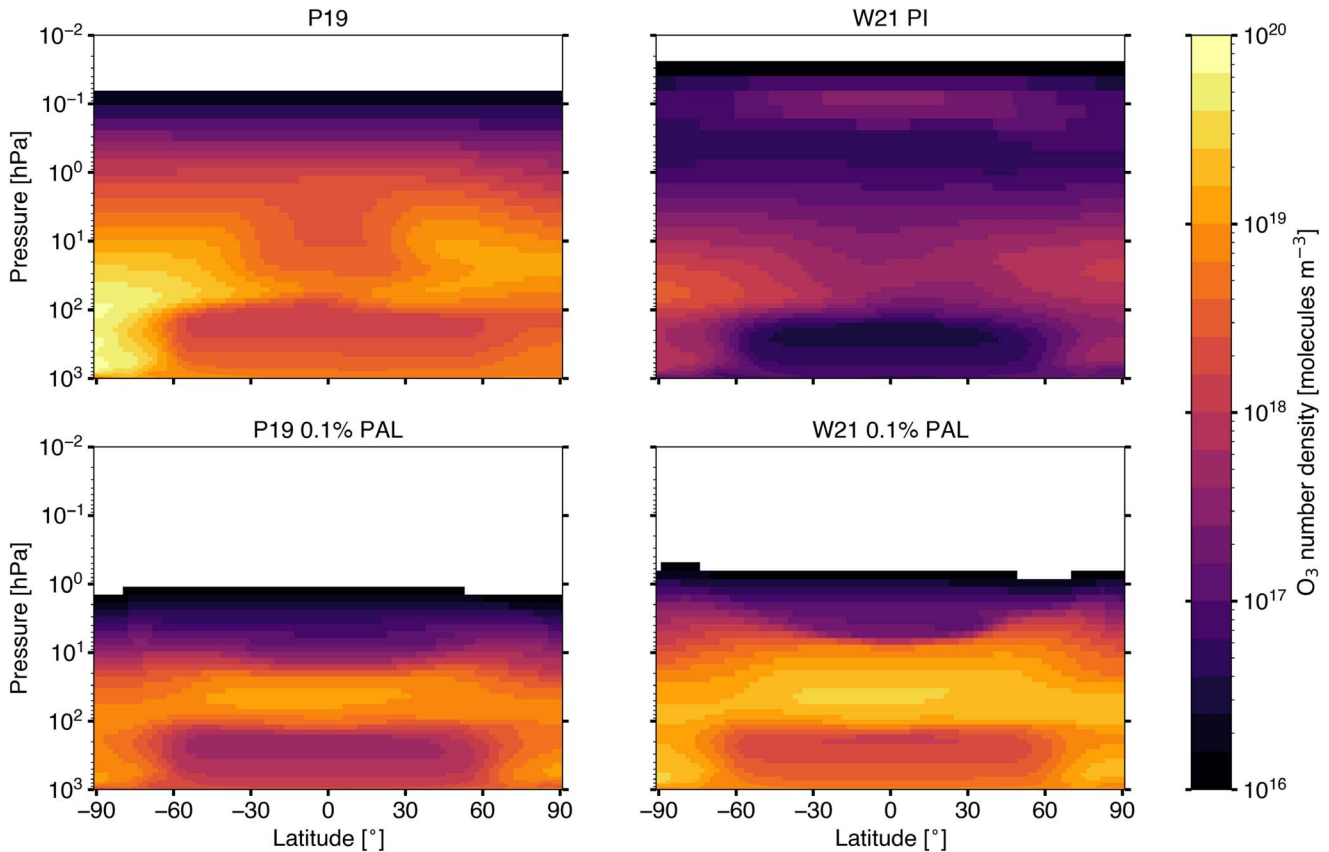
Figure 3. The P19 (left column) and W21 (right column) irradiation scenarios are compared to each other for the PI (top row) and 0.1% PAL (bottom row) cases. The zonal mean (average over longitude) of the O_3 number density is shown, with latitude in degrees on the horizontal axis and pressure in hectopascals on the vertical axis. The white regions show where the number density has dropped below 10^{16} molecules m^{-3}.

atmosphere. This reduces the rate of catalytic destruction reactions and allows O_3 formation to occur faster.

Figure 5 displays the longitudinal and latitudinal variation of the O_3 column for the simulations averaged over the last 10 years of each scenario. O_3 is inhomogeneously distributed horizontally, which highlights the importance of using 3D models. The P19 PI simulation has a global mean O_3 column of 1310 Dobson units (DU; approximately 4.4 times Earth's global mean value of $\approx$300 DU, where 1 DU = 2.687×10^{20} molecules m^{-2}), while the W21 PI simulation predicts a global mean O_3 column of 50 DU. Both of the O_3 column maxima, at 7152 DU and 117 DU for the P19 PI and W21 PI simulations, respectively, occur near the southern pole.

Figure 6 shows the total range of O_3 columns produced across the atmospheric latitude–longitude grid against the O_2 volume mixing ratio. The O_3 column depends on the incident UV radiation, O_2 concentration, atmospheric pressure, temperature, and transport, as well as the rates of destruction. In the W21 PI case, the UV radiation is absorbed high in the atmosphere where the pressure is low, so little O_3 is produced and the O_x (O + O_3) is primarily in O. As O_2 is decreased, the O_3 column increases. In contrast, in the P19 simulations, which have larger incoming fluxes of UV, as O_2 increases above 1% PAL, the O_3 column increases, similar to the relationship on Earth. Both of these data sets are rather different when compared to previous results that have simulated the atmospheres of planets around late M dwarf stars (e.g., Rugheimer & Kaltenegger 2018; Kozakis et al. 2022; although note that the total instellation in those simulations were set to Earth's

modern value). While there are likely many interacting parameters which will cause dissimilar O_3 column predictions, the very large discrepancies with 1D models could be due to 3D transport. This seems plausible because Braam et al. (2023) reported a stratospheric circulation in simulations of a terrestrial Proxima Centauri b scenario, in which the winds move O_3 from the dayside to the nightside, with similar circulation effects occurring in the WACCM6 simulations here (the large-scale dynamics of the atmosphere will be explored in future work).

3.2. Transmission Spectra

In Figure 7 we show idealized transmission spectra between 0.1 and 11 μm generated using the WACCM6 simulations with PSG (excluding the non–tidally locked cases). The model date chosen for the transit is arbitrary. Because there are time-dependent fluctuations for several variables in the WACCM6 simulations (e.g., clouds and chemical mixing ratios), we could have investigated time variability in the transmission spectra. However, Fauchez et al. (2022) showed that such variability is within the measurement uncertainties of JWST. The spectra are binned to approximate a resolving power of $R = 250$ to show detail in spectral features, where $R = \lambda/\Delta\lambda$, λ is the wavelength, and $\Delta\lambda$ is width of the wavelength bin. A 5 ppm error bar corresponding to the lowest achievable noise with JWST instruments, which may be between 5 and 20 ppm as calculated by Matsuo et al. (2019), Schlawin et al. (2020), Schlawin et al. (2021), and Rustamkulov et al. (2022), is indicated.
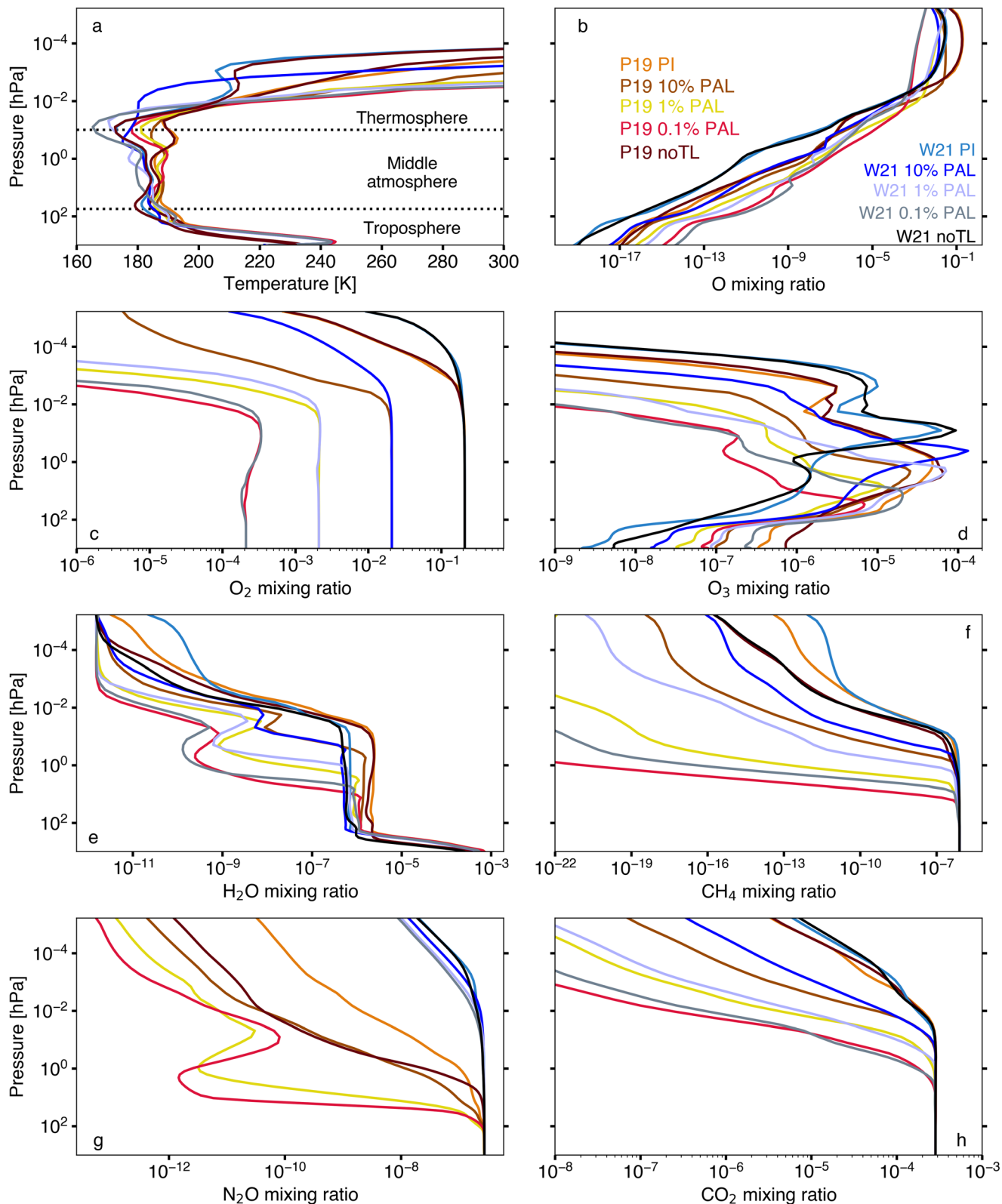
Figure 4. The global mean temperature (a) is plotted against pressure for the P19 PI (orange), P19 noTL (dark red), P19 10% PAL (brown), P19 1% PAL (yellow), and P19 0.1% PAL (red) simulations, and the W21 PI (light blue), W21 noTL (black), W21 10% PAL (blue), W21 1% PAL (lilac), and W21 0.1% PAL (gray) simulations. The globally averaged mixing ratios for O (b), O_2 (c), O_3 (d), H_2O (e), CH_4 (f), N_2O (g), and CO_2 (h), are also shown.

The differences in the effective altitude of O_3 spectral features between the P19 PI (orange) and W21 PI (light blue) transmission spectra are −4 km, +20 km, +16 km, and +18 km for the 0.25, 0.6, 4.71, and 9.6 μm O_3 features, respectively.

Despite the W21 PI simulation having an O_3 column $\approx$ 26 times lower than the P19 PI simulation, the W21 PI UV feature (centered at 0.25 μm) due to the HaB (0.2–0.31 μm) actually has the largest effective altitude between 0.2 and 0.3 μm of all
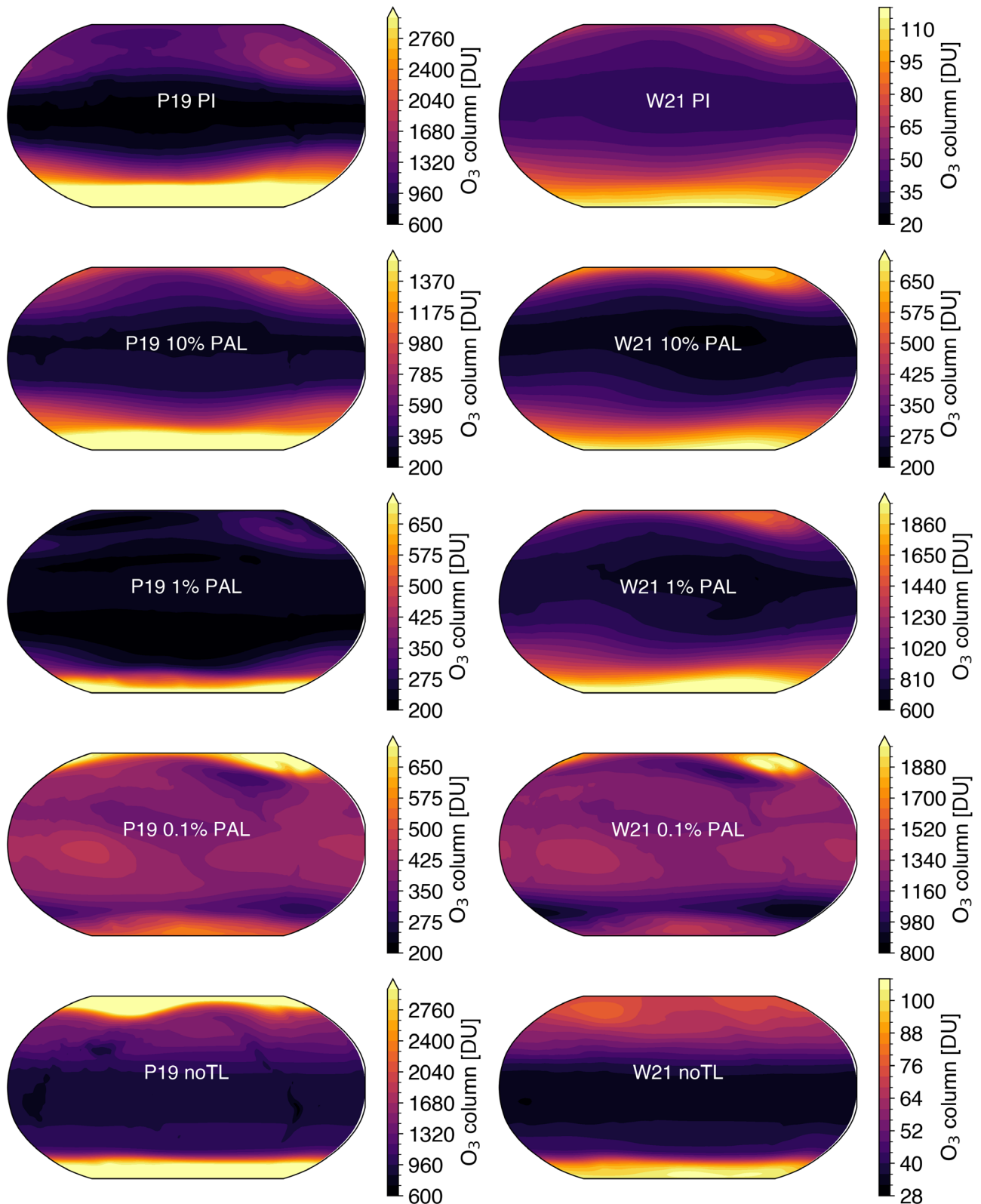
Figure 5. The O_3 column in DU across the simulation's latitudinal and longitudinal grid is plotted for all the simulations used in this work (the P19 scenarios are in the left column and the W21 scenarios are in the right column). 1 DU is equal to 2.6867×10^{20} molecules m^{-2}. In all simulations, O_3 column maxima occur at high latitudes. The substellar point for the tidally locked cases is at 180° longitude and 0° latitude on Earth's coordinate grid (in the center of each Robinson projection). Note that the color bars are extended for some simulations in order to show the O_3 column structure in each scenario. Each panel has a different color bar range.

the simulations. This is because the HaB saturates quickly and the W21 PI atmosphere has more total O_3 than the P19 PI atmosphere above ≈ 0.5 hPa. Between 0.3 and 0.35 μm, the

temperature dependence of the HaBs and HuBs reduces the effective height of the W21 PI transmission spectra due to the colder middle atmosphere in the W21 PI simulation. At 0.6 μm,
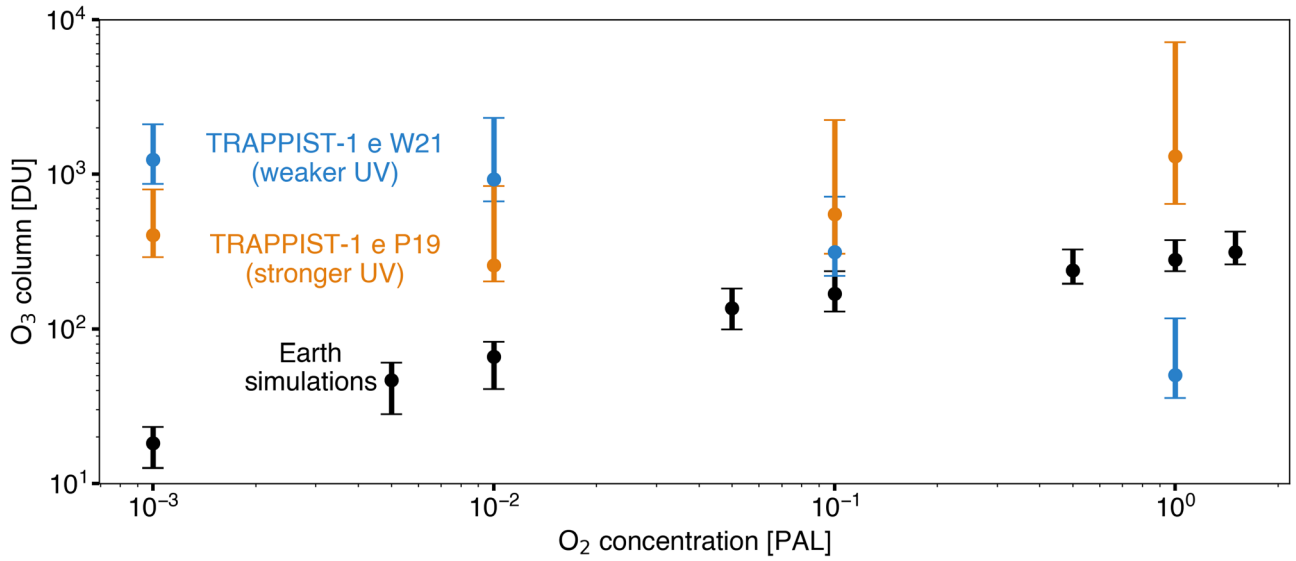
Figure 6. The oxygen (O_2) concentration is shown against the ozone (O_3) column in each simulation (orange for P19 scenarios and blue for W21 scenarios). The "error bar" lines show the range between the minimum and maximum O_3 columns in each simulation. The circular dots show the mean O_3 columns. The O_3 columns simulated by WACCM6 for Earth, from Cooke et al. (2022), are shown in black for comparison.
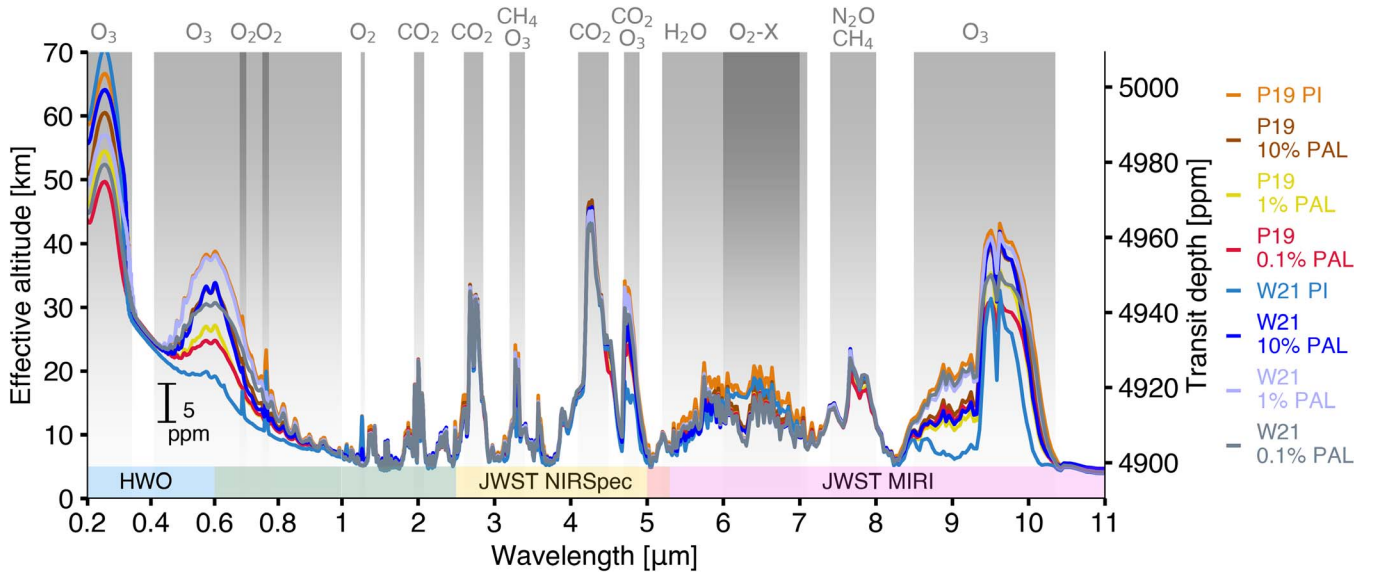
Figure 7. The transmission spectrum atmospheric effective altitude is plotted against wavelength between 0.2 and 11 μm for the P19 PI (orange), P19 10% PAL (brown), P19 1% PAL (yellow), and P19 0.1% PAL (red) simulations, and the W21 PI (light blue), W21 10% PAL (blue), W21 1% PAL (lilac), and W21 0.1% PAL (gray) simulations. The non–tidally locked cases are excluded for clarity, but show little differences compared to the equivalent tidally locked case. The transit depth, in terms of contrast with respect to the star, is indicated on the right vertical axis in units of ppm. The spectra are binned to a spectral resolving power of $R = 250$. Spectral features are indicated in gray. The wavelength range of the proposed Habitable Worlds Observatory (HWO; blue shaded region), and that of the JWST NIRSpec instrument (yellow shaded region), are shown. They overlap in the green shaded region. The wavelength range of the JWST MIRI instrument is indicated in the magenta shaded region. The wavelength spacing between 0.2 and 1 μm is changed between 1 and 11 μm in order to show the UV and visible regions clearly. The black bar represents the uncertainty that would be present on a measurement that has reached the noise floor of the instrument, where the noise floor is indicated as 5 ppm. Note this error bar is an estimate of the performance of the telescope and does not indicate a measurement.

a significant detection of O_3 with JWST in the W21 PI simulation scenario would be improbable given that the noise floor is comparable to the height of the feature. Therefore, assuming that the W21 spectrum is closest to the true spectrum of TRAPPIST-1, or the case that the true stellar UV emission is weaker, a null detection of the 0.6 μm O_3 feature should not rule out the presence of O_2 abundances at levels as high as the present-day Earth. For H_2O, the spectral features are stronger in the P19 PI transmission spectra compared to W21 PI by up to 8 km, which is the result of a larger number density of H_2O in the middle atmosphere. Despite the difference in temperature

and O_3 number density profiles between the noTL simulation and PI simulations, the transmission spectra are remarkably similar (within a ±4 km effective altitude, not shown for clarity). The P19 0.1% PAL transmission spectrum (red) produces a quantitatively similar transmission spectrum feature at 9.6 μm to the W21 PI simulation (light blue), even though there is a 1000 times difference in the O_2 mixing ratio between the two cases. The same can be said of the following pairs at 9.6 μm: W21 1% PAL and P19 PI; W21 0.1% PAL and P19 1% PAL; and W21 10% PAL and P19 10% PAL. There is a noticeable difference between the spectra at 4.71 and 9 μm, but
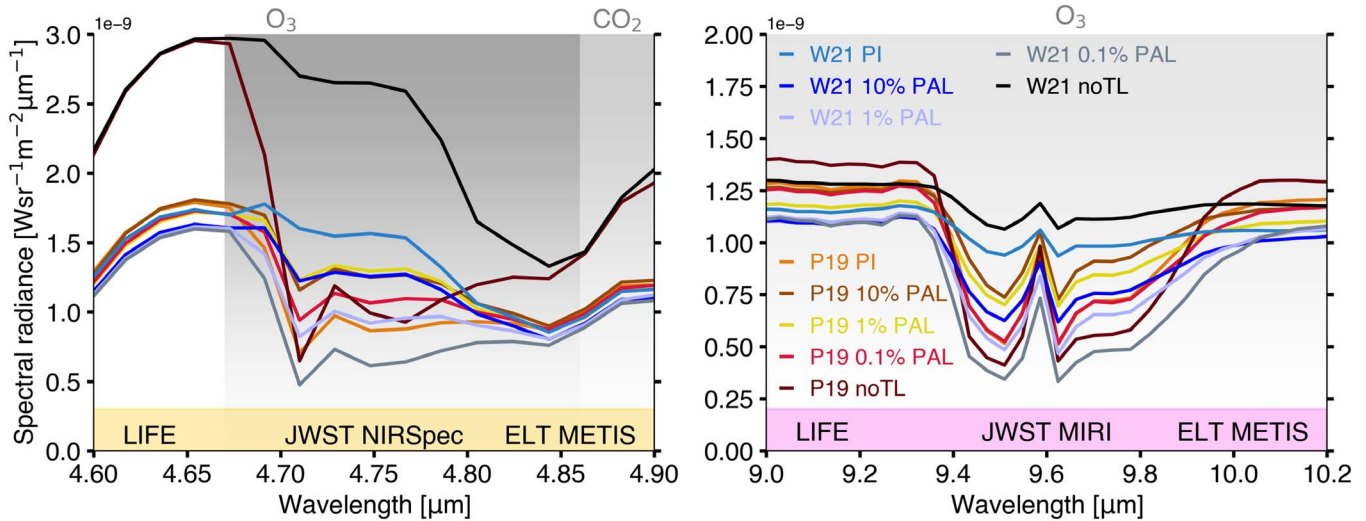
Figure 8. The left panel shows the PSG simulations of planetary spectral radiance from emission spectra focused on the 4.71 μm O_3 feature (which overlaps with a CO_2 feature, both shown by the gray shaded regions) for the P19 PI (orange), P19 10% PAL (brown), P19 1% PAL (yellow), and P19 0.1% PAL (red) simulations, and the W21 PI (light blue), W21 noTL (black), W21 10% PAL (blue), W21 1% PAL (lilac), and W21 0.1% PAL (gray) simulations. The right panel shows the same for the 9.6 μm O_3 feature, shown by the gray shaded region. Telescopes and their instruments which may be able to probe atmospheres in the infrared include: the Extremely Large Telescope (ELT; Brandl et al. 2021) METIS instrument, the Large Interferometer for Exoplanets (LIFE; Konrad et al. 2022), and the JWST (Morley et al. 2017) NIRSpec and MIRI instruments.

this would require reaching the most optimistic 5 ppm noise floor in order to demonstrate that the two O_2 scenarios are distinguishable when there exist uncertain stellar UV flux estimates. Also note that the effective height of the $O_2 - X$ collision-induced absorption feature at 6.4 μm (see Fauchez et al. 2020b, for more details) is up to 7 km shallower when O_2 is at 0.1% PAL in the P19 and W21 scenarios, compared to the PI cases.

3.3. Emission Spectra

In Figure 8 we show the emission spectra from each simulation for the atmospheric absorption O_3 features at 4.71 and 9.6 μm at 90° orbital phase (the maximum planet–star separation as viewed in an edge-on system with a circular orbit). The 4.71 μm feature overlaps with a CO_2 feature, but O_3 is the dominant absorber at 4.71 μm. The P19 PI simulation (orange) predicts higher O_3 columns than the W21 PI case (light blue); hence, the depth of the features relative to the continuum in the W21 PI case are weaker than the P19 PI scenario by a factor of 4.2 and 4.5 at 4.71 μm and 9.6 μm, respectively. With respect to the P19 0.1% PAL emission spectrum (red), the P19 PI emission spectrum (orange) has a greater depth by a factor of 1.3 and 1.1 at 4.71 and 9.6 μm, respectively, even though the P19 PI simulation has a mean O_3 column which is 3.2 times higher than the P19 0.1% PAL simulation (1310 DU versus 405 DU). The 3D effects are important here because the largest O_3 columns are found at the poles, but PSG is integrating over the whole observable disk. At 4.71 μm, the noTL absorption features are deeper than the tidally locked PI cases by a factor of 2.0 and 1.2 in the P19 and W21 scenarios, respectively. At 9.6 μm, these values are 1.2 and 1.0. In terms of the relative depths of O_3 features shown in Figure 8, increasing depth is generally shown with increasing mean O_3 column (see Figure 5).

The tidally locked simulations exhibit strong convection and high clouds around the substellar point, whereas the P19 noTL simulation has mainly low clouds with comparatively little high cloud coverage. Therefore, this results in the P19 noTL

simulation (dark red) having the deepest O_3 emission spectral features.

It is important to note that other orbital phases may show quantitatively different results because variability in spectral features may occur due to climate variations throughout the orbit (e.g., Cooke et al. 2023). Additionally, longer-term variations may be expected due to the possible presence of a "longitudinally asymmetric stratospheric oscillation" (Cohen et al. 2022).

4. Discussion

We have demonstrated that large differences in assumed stellar UV spectra can lead to different predictions for the strength of O_3 spectral features. These spectral features may overlap at an assumed minimum observational uncertainty of 5 ppm, despite the fact that the O_2 concentration differs by factors of up to 1000. In this section, we compare our results to previous work, consider known uncertainties, and discuss work that should be done in preparation for future exoplanet observations.

1D photochemical modeling of M dwarf terrestrial exoplanet atmospheres has demonstrated that CH_4 and N_2O could have greater abundances in the middle atmosphere compared to the modern Earth's atmosphere (e.g., Segura et al. 2005; Wunderlich et al. 2019), which we also find in our WACCM6 simulations of TRAPPIST-1 e (see Figure 4). Teal et al. (2022) showed changes of over two orders of magnitude in the middle atmosphere O_3 mixing ratios when modeling a modern Earth-like exoplanet that receives 1 $S_\oplus$ of irradiation around GJ 176 (an M2.5V star), but with various UV irradiation scenarios. They derived transmission spectra predictions from their atmospheric simulations and found the maximum transit depth differences to be <2 ppm, which is below the noise floor (5 ppm or greater) for JWST. This is in contrast to the W21 PI and P19 PI transmission spectra results shown here, where the strengths of the estimated O_3 features here are distinct at the 5 ppm level. While different atmospheric modeling methods are used in Teal et al. (2022) compared with this work, the difference in observational significance is primarily due to the

size of the stars modeled: the radius of GJ 176 is 0.45 $R_{\odot}$, and the radius of TRAPPIST-1 is 0.1192 $R_{\odot}$. Teal et al. (2022) also demonstrated that hazy Archean Earth atmospheres were more sensitive to changes in the incoming UV spectra compared to the modern Earth's atmosphere, which warrants future investigations for how uncertainties in the UV spectrum of the host star affect hazy atmospheres in 3D models.

In terms of 3D modeling, the THAI series (Fauchez et al. 2020a; Sergeev et al. 2022a; Turbet et al. 2022) has investigated the climate of TRAPPIST-1 e using four different 3D global climate models, assuming either an N_2- or CO_2-dominated atmosphere and not including interactive chemistry, where the composition evolves depending on chemical and photochemical reactions. The surface temperatures in the WACCM6 simulations are similar although slightly lower (219–231 K global mean compared to 230–240 K in the THAI simulations. See Appendix A and Figure 9 for more details), which may be due to differences in assumptions regarding the surface (including the distribution of the continents and the fact that an interactive ocean is used here, in contrast to a slab ocean with no meridional heat transport) or the composition of the atmosphere. With a previous version of WACCM (CESM1), Chen et al. (2019) investigated a planet with a 43.87 day orbital period around a star with an effective temperature of 4000 K and an insolation of 1.9 $S_{\oplus}$, as opposed to the 0.66 $S_{\oplus}$ used here, and assessed the impact of uncertain host-star UV flux on the atmosphere. Chen et al. (2019) showed that two different spectra (representing a quiescent and an active M dwarf star) impacted the middle atmospheric concentrations of O_3, OH, N_2O, CH_4, and H_2O. They calculated transmission spectra for the two simulated atmospheres, finding that the only observable difference was for the O_3 feature at 9.6 μm (although the UV O_3 feature is not shown in their Figure 11). On the other hand, the transmission spectra simulations shown here in Figure 7 display noticeable spectral differences for O_3 at 0.25, 0.6, 4.7, 9.0, and 9.6 μm, as well as at 13–14 μm, and for H_2O between 5 and 6 μm. The differences in the predicted observations between our work and that of Chen et al. (2019) likely arise due to the differences in exoplanetary system setup, the different stellar spectra, and the calculated lower O_3 columns from Chen et al. (2019), compared to the simulated atmospheres here. 43.87 days is in the "slow rotator" regime (for the definition of tidally locked rotation regimes see Haqq-Misra et al. 2018), and 6.1 days for TRAPPIST-1 e can correspond to either the "Rhines rotator" or "fast rotator" regimes (Sergeev et al. 2022b). Thus, our results, alongside those from Chen et al. (2019), demonstrate that 3D modeling results are sensitive to the choice of the assumed stellar UV spectra for potentially habitable tidally locked exoplanets across early and late M dwarf stars and different rotation periods. Future work should also investigate the influence of orbital perturbations away from a synchronous 1:1 spin–orbit resonance (e.g., Chen et al. 2023) on composition.

The anisotropy of chemical molecules will affect the emission spectra and photometry of terrestrial exoplanets, by modulating when the exoplanet is brightest and dimmest at particular wavelengths (Selsis et al. 2011; Chen et al. 2018). The phase-curve photometric amplitude, and where the maximum brightness occurs during the orbit, depends on the particular rotation regime within which the exoplanet exists (Haqq-Misra et al. 2018). Thermal emission features are influenced by molecular abundance, the atmospheric temperature, and the temperature difference between the emitting and absorbing regions (e.g., for Earth, infrared emission emanates from the troposphere, while the absorbing region is the O_3 layer in the stratosphere). This temperature difference is larger for M dwarf exoplanets which exhibit a less pronounced stratospheric temperature inversion due to lower incident UV emission for the same total instellation.

Note that detecting O_3 will be difficult with JWST within the nominal 5 yr mission lifetime (although JWST is expected to continue science operations for at least 10 yr), even for a modern Earth scenario (Lin et al. 2021), and Fauchez et al. (2019) found that gases other than CO_2 may require hundreds or thousands of transits to be detectable. Simulations of high-resolution observations with the extremely large class of telescopes indicate that O_2 at 0.76 μm may be detectable in the case of TRAPPIST-1 e within ∼100 transits (Snellen et al. 2013; Rodler & López-Morales 2014; Serindag & Snellen 2019).

The derived Mega-MUSCLES spectrum of TRAPPIST-1 (W21) is constrained by more observations than the P19 spectrum, but both spectra have significant flux uncertainties. While neither spectrum used in this study is likely to represent the true stellar irradiation environment of TRAPPIST-1 e wholly, there are at least observational constraints on the "ground truth" of its parent star's spectrum. For many planetary systems, there will only be estimates from stellar models, and this will cause significant problems for predicting the photochemical environment of potentially habitable exoplanets. Furthermore, in each wavelength bin, we have assumed that the flux does not vary with time. Due to M dwarf stellar activity, such an assumption is unlikely to be accurate (Loyd et al. 2018). The O_3 abundance will be perturbed by the inclusion of incident stellar flares (Segura et al. 2010; Tilley et al. 2019; Chen et al. 2021; Ridgway et al. 2023) which we have not investigated here. Based on previous results, it seems that stellar flares will exacerbate the interpretation of observed spectra, so future work on incoming UV uncertainties could evaluate the additional impact of stellar flares. The present modeling uncertainties in the O_2–O_3 nonlinear relationship arising from differences in predictions between 1D and 3D models (Cooke et al. 2022; Kozakis et al. 2022; Yassin Jaziri et al. 2022; Ji et al. 2023) will compound this issue. In addition to previous work, our simulations, which focus on the specific target of TRAPPIST-1 e, further motivates the need for a dedicated next-generation observatory with UV capabilities to characterize exoplanet host stars.

UV flux measurements from a telescope such as the ∼6 m UV/VIS/NIR Telescope (currently referred to as the HWO) that was recommended by the Decadal Survey (National Academies of Sciences, and Engineering, & Medicine 2021) will aid the interpretation of observed exoplanet spectra and help to infer the concentration of O_2 and trace gases in the atmosphere without direct measurements (Kozakis et al. 2022). However, this telescope is not expected to be operational until the late 2030s at the earliest. Determining the EUV fluxes from a host star (which will require a dedicated observatory; Youngblood et al. 2019) will also provide important information about atmospheric escape, habitability, and help to examine the atmospheric history of the exoplanets in the system.

Before next-generation telescopes are online, there are other clues available to characterize oxygenated terrestrial atmospheres if the interpretation of the spectral features (e.g., O_3) leaves degeneracies in the parameter space between O_2 concentration, O_3 concentration, UV irradiation, and O_3 depleting catalytic

cycles. For example, the major differences between the P19 PI and the P19 0.1% PAL transmission spectra are between the H_2O, O_2, and O_3 features. Moreover, the estimated intersimulation trends with wavelength in transmission spectra are not mirrored in emission spectra predictions. Namely, the depth relative to the continuum in emission spectra for O_3 at 4.71 and 9.6 μm contrasts with the relative strength of associated transmission spectrum features between the simulations. This means that if both transmission spectra and emission spectra are acquired with adequate precision, multiwavelength observations combined with atmospheric retrieval methods (Quanz et al. 2021) will be useful when delineating between possible atmospheric composition scenarios. Nevertheless, Batalha et al. (2018) showed that confident estimates on atmospheric composition from emission spectra observed with JWST MIRI LRS will prove difficult to achieve for temperate exoplanets, using TRAPPIST-1 f as an example.

Finally, future modeling work should explore the impact of chemical boundary conditions on simulated transmission and emission spectra. For example, the choice of boundary conditions, such as the upward flux and abundances of species in the HO_x, NO_x, ClO_x, and BrO_x families, will not only affect the O_3 distribution but also the atmospheric temperature and incoming radiation. Provided the atmospheric profile of O_3 derived from atmospheric retrievals is well constrained, by assuming minimal and maximal O_3 catalytic cycle destruction, limits could be placed on O_2.

5. Conclusions

For the first time using a 3D chemistry climate model (WACCM6) to simulate TRAPPIST-1 e (assuming an initial Earth-like composition) and including two different incoming UV spectra, we demonstrated that using a single observed O_3 feature outside of the UV range to extrapolate to undetected molecules, such as O_2, will lead to degeneracies over multiple orders of magnitude in the parameter space for atmospheric composition. The UV spectrum in both of the incoming stellar spectra varies by up to a factor of ≈ 500 for important photolysis bands, and up to ≈ 5000 for individual wavelength bins. While the atmospheric columns of many species (including O_2 and CO_2) are virtually unaffected by the difference between the two spectra, for an O_2 mixing ratio of 0.21, the O_3 columns differ by a factor of 26 due to different O_3 production rates that are sensitive to the incoming spectrum. Consequently, the associated O_3 transmission spectral features differ in effective altitude by up to 20 km, while the O_3 features in emission spectra differ by a factor of up to 4.5 in relative

depth. One implication is that a nondetection of O_3 at visible wavelengths may not indicate the absence of an oxygenated atmosphere. Furthermore, tidal locking of the model results in substantially different emission spectral features which are shallower relative to the emission continuum.

Without the direct detection of O_2, additional context for determining the oxygenation state of the atmosphere can be gained from either (1) future missions that are able to characterize the UV spectra of faint stars better, or (2) sensitive direct imaging observations combined with transmission spectra observations targeting individual features.

Appendix A
Surface Temperatures

The time-averaged surface temperatures for all the simulations (see Table 3 for simulation details) are shown in Figure 9. On time average, the global mean surface temperatures are between 219 and 231 K, with the minima ranging between 171 and 180 K, and the maxima ranging between 252 and 277 K. The P19 and W21 noTL simulations are everywhere colder than 273 K, while all other simulations do have some areas of the surface which are warmer than 273 K (the freezing point of water under 1 bar of atmospheric pressure).
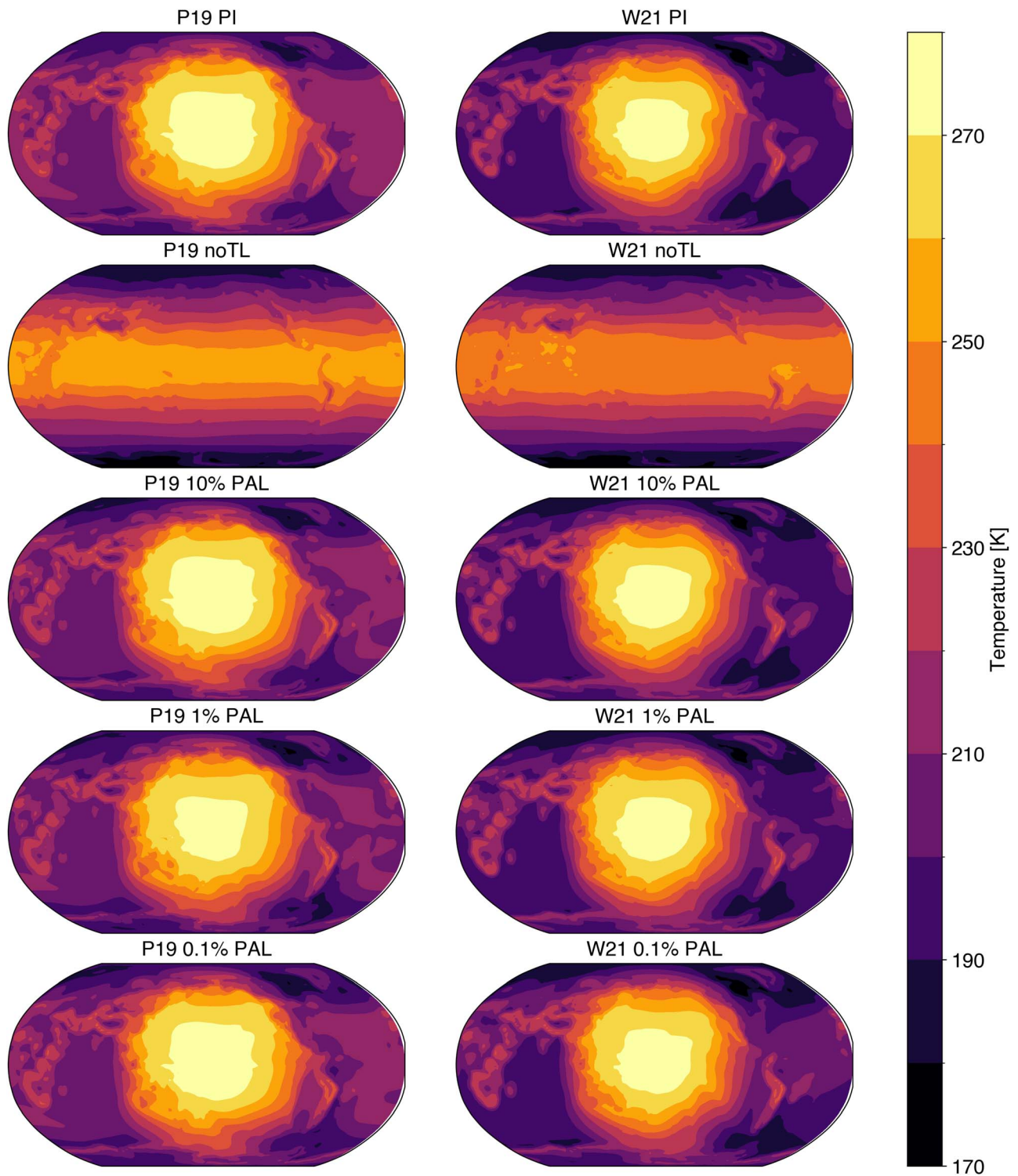
Figure 9. The surface temperatures in kelvin are shown for the P19 (left column) and W21 (right column) PI, noTL, 10% PAL, 1% PAL, and 0.1% PAL scenarios. In the tidally locked cases, a relatively warm region exists around the substellar point, which receives constant irradiation. The substellar point for the tidally locked cases is at 180° longitude and 0° latitude (in the center of each Robinson projection). In the P19 and W21 noTL cases, the substellar point moves because there is a diurnal cycle. These simulations have the coldest surface temperatures (171 and 170 K, respectively), but the smallest range in surface temperatures.

Appendix B
Water Vapor and High Clouds

Figure 10 shows the water vapor (H$_2$O) column for the PI and 0.1% PAL simulations for both the P19 and W21 scenarios. The H$_2$O column is predominantly situated around and above the substellar point. This is because the incoming solar radiation heats the surface, and water vapor evaporates. The ascending air parcels carry the water vapor upwards, where the parcels cool and form clouds.

Figure 11 shows the high cloud fraction for the PI and 0.1% PAL simulations for both the P19 and W21 scenarios. High clouds are defined as clouds at pressures less than 400 hPa. Clouds, through shortwave (incoming solar radiation) and longwave (outgoing terrestrial radiation) forcing, provide a net warming of 8–12 W m^{-2} in the tidally locked scenarios, and 5–7 W m^{-2} in the non–tidally locked scenarios.
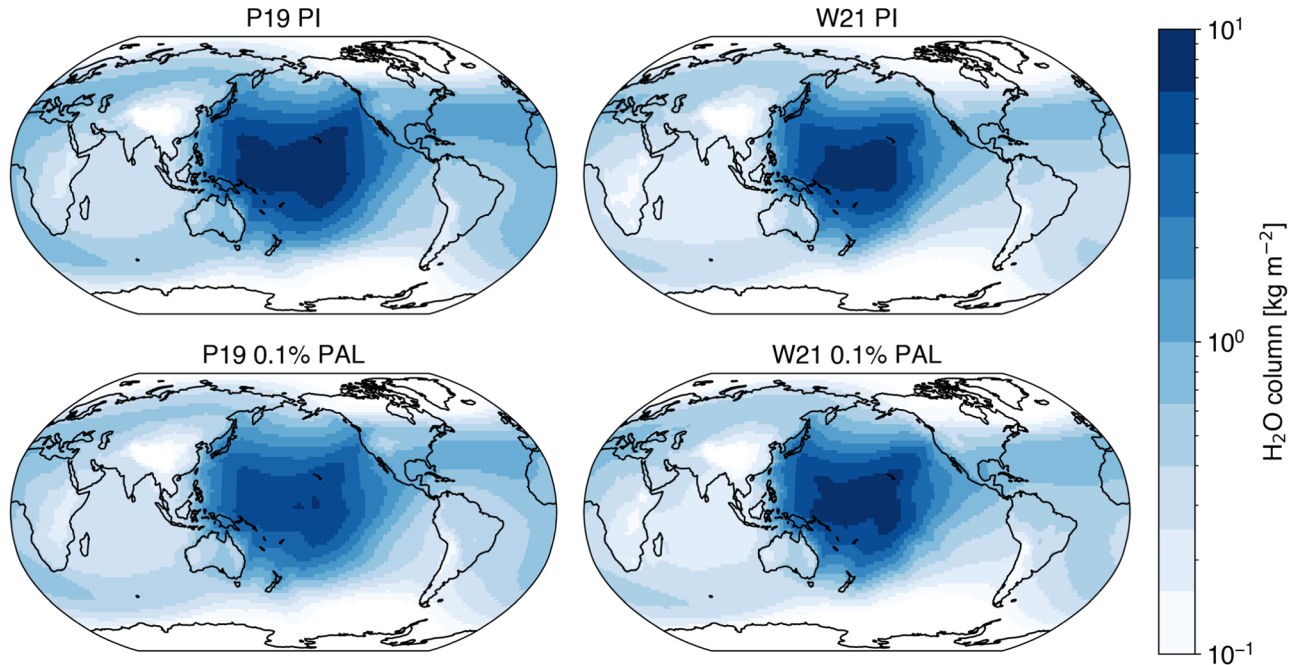
Figure 10. The H$_2$O column, given in terms of kgm^{-2}, is shown for the PI and 0.1% PAL simulations in the P19 (left) and W21 (right) scenarios. White shows a relatively low H$_2$O column, while blue shows relatively large amounts of H$_2$O column. For reference, Earth's H$_2$O column reaches a peak of about 50 kg m^{-2}.
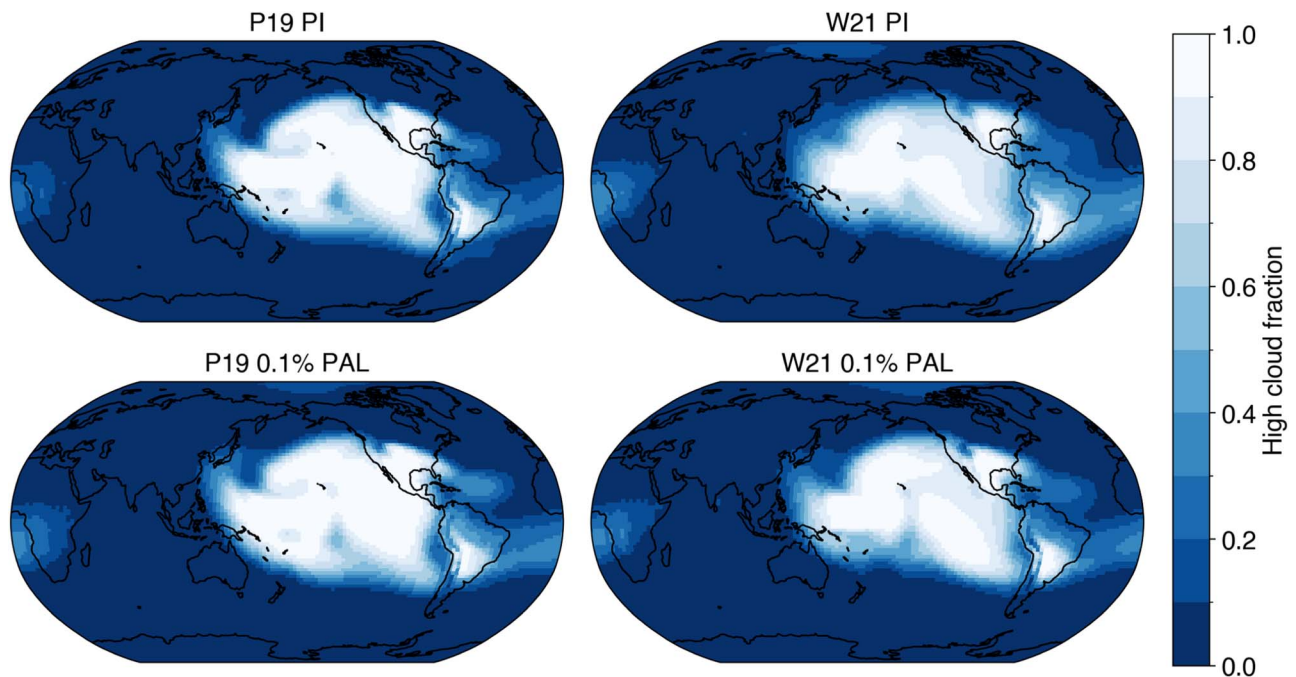
Figure 11. The high cloud fraction, where high clouds are specified as clouds at pressures below 400 hPa, is shown for the PI and 0.1% PAL simulations in the P19 (left) and W21 (right) scenarios. Blue shows low cloud fraction, while white shows large amounts of cloud coverage. Clouds provide a net warming in the tidally locked scenarios.

14

ORCID iDs

G. J. Cooke ⓘ https://orcid.org/0000-0001-6067-0979
D. R. Marsh ⓘ https://orcid.org/0000-0001-6699-494X
C. Walsh ⓘ https://orcid.org/0000-0001-6078-786X
A. Youngblood ⓘ https://orcid.org/0000-0002-1176-3391

References

Agol, E., Dorn, C., Grimm, S. L., et al. 2021, PSJ, 2, 1
Akeson, R. L., Chen, X., Ciardi, D., et al. 2013, PASP, 125, 989
Baron, E., & Hauschildt, P. H. 2007, A&A, 468, 255
Batalha, N. E., Lewis, N. K., Line, M. R., Valenti, J., & Stevenson, K. 2018, ApJL, 856, L34
Bourrier, V., Ehrenreich, D., Wheatley, P. J., et al. 2017, A&A, 599, L3
Braam, M., Palmer, P. I., Decin, L., et al. 2022, MNRAS, 517, 2383
Braam, M., Palmer, P. I., Decin, L., Cohen, M., & Mayne, N. J. 2023, MNRAS, 526, 263
Brandl, B., Bettonvil, F., van Boekel, R., et al. 2021, Msngr, 182, 22
Brasseur, G. P., & Solomon, S. 2005, Aeronomy of the Middle Atmosphere: Chemistry and Physics of the Stratosphere and Mesosphere (Dordrecht: Springer)
Caldas, A., Leconte, J., Selsis, F., et al. 2019, A&A, 623, A161
Chapman, S. 1930, The London, Edinburgh, and Dublin Philosophical Magazine and Journal of Science, 10, 369
Chen, H., Li, G., Paradise, A., & Kopparapu, R. 2023, ApJL, 946, L32
Chen, H., Wolf, E. T., Kopparapu, R., Domagal-Goldman, S., & Horton, D. E. 2018, ApJL, 868, L6
Chen, H., Wolf, E. T., Zhan, Z., & Horton, D. E. 2019, ApJ, 886, 16
Chen, H., Zhan, Z., Youngblood, A., et al. 2021, NatAs, 5, 298
Cohen, M., Bollasina, M. A., Palmer, P. I., et al. 2022, ApJ, 930, 152
Cooke, G. J., Marsh, D. R., Walsh, C., Black, B., & Lamarque, J. F. 2022, RSOS, 9, 211165
Cooke, G. J., Marsh, D. R., Walsh, C., Rugheimer, S., & Villanueva, G. L. 2023, MNRAS, 518, 206
Costa, E., Méndez, R. A., Jao, W. C., et al. 2006, AJ, 132, 1234
Delrez, L., Gillon, M., Triaud, A. H. M. J., et al. 2018, MNRAS, 475, 3577
Dong, C., Jin, M., Lingam, M., et al. 2018, PNAS, 115, 260
Eager-Nash, J. K., Reichelt, D. J., Mayne, N. J., et al. 2020, A&A, 639, A99
Emmons, L. K., Schwantes, R. H., Orlando, J. J., et al. 2020, JAMES, 12, e2019MS001882
Fauchez, T. J., Turbet, M., Villanueva, G. L., et al. 2019, ApJ, 887, 194
Fauchez, T. J., Turbet, M., Wolf, E. T., et al. 2020a, GMD, 13, 707
Fauchez, T. J., Villanueva, G. L., Schwieterman, E. W., et al. 2020b, NatAs, 4, 372
Fauchez, T. J., Villanueva, G. L., Sergeev, D. E., et al. 2022, PSJ, 3, 213
Froning, C. S., Kowalski, A., France, K., et al. 2019, ApJL, 871, L26
Gillon, M., Triaud, A. H. M. J., Demory, B.-O., et al. 2017, Natur, 542, 456
Godolt, M., Grenfell, J. L., Hamann-Reinus, A., et al. 2015, P&SS, 111, 62
Gordon, I. E., Rothman, L. S., Hill, C., et al. 2017, J. Quant. Spec. Radiat. Transf., 203, 3
Grenfell, J. L., Gebauer, S. V., Paris, P., Godolt, M., & Rauer, H. 2014, P&SS, 98, 66
Grimm, S. L., Demory, B.-O., Gillon, M., et al. 2018, A&A, 613, A68
Haqq-Misra, J., Wolf, E. T., Joshi, M., Zhang, X., & Kopparapu, R. K. 2018, ApJ, 852, 67
Hauschildt, P. H. 1993, J. Quant. Spec. Radiat. Transf., 50, 301
Hauschildt, P. H., & Baron, E. 2006, A&A, 451, 273

Ji, A., Kasting, J. F., Cooke, G. J., Marsh, D. R., & Tsigaridis, K. 2023, RSOS, 10, 230056
Kaltenegger, L. 2017, ARA&A, 55, 433
Konrad, B. S., Alei, E., Quanz, S. P., et al. 2022, A&A, 664, A23
Kozakis, T., Mendonça, J. M., & Buchhave, L. A. 2022, A&A, 665, A156
Leger, A., Pirre, M., & Marceau, F. J. 1993, A&A, 277, 309
Lin, Z., MacDonald, R. J., Kaltenegger, L., & Wilson, D. J. 2021, MNRAS, 505, 3562
Loyd, R. O. P., France, K., Youngblood, A., et al. 2018, ApJ, 867, 71
Luger, R., Sestovic, M., Kruse, E., et al. 2017, NatAs, 1, 0129
Matsuo, T., Greene, T. P., Johnson, R. R., et al. 2019, PASP, 131, 124502
Meadows, V. S., Reinhard, C. T., Arney, G. N., et al. 2018, AsBio, 18, 630
Morley, C. V., Kreidberg, L., Rustamkulov, Z., Robinson, T., & Fortney, J. J. 2017, ApJ, 850, 121
National Academies of SciencesEngineering, and Medicine 2021, Pathways to Discovery in Astronomy and Astrophysics for the 2020s (Washington, DC: National Academies Press)
Peacock, S. 2020, Habitable Zones and M dwarf Activity across Time ("HAZMAT,") STScI/MAST doi:10.17909/t9-j6bz-5g89
Peacock, S., Barman, T., Shkolnik, E. L., Hauschildt, P. H., & Baron, E. 2019, ApJ, 871, 235
Proedrou, E., & Hocke, K. 2016, EP&S, 68, 96
Quanz, S. P., Absil, O., Benz, W., et al. 2021, ExA, 54, 1197
Ridgway, R. J., Zamyatina, M., Mayne, N. J., et al. 2023, MNRAS, 518, 2472
Rodler, F., & López-Morales, M. 2014, ApJ, 781, 54
Rugheimer, S., & Kaltenegger, L. 2018, ApJ, 854, 19
Rugheimer, S., Kaltenegger, L., Zsom, A., Segura, A., & Sasselov, D. 2013, AsBio, 13, 251
Rustamkulov, Z., Sing, D. K., Liu, R., & Wang, A. 2022, ApJL, 928, L7
Schlawin, E., Leisenring, J., McElwain, M. W., et al. 2021, AJ, 161, 115
Schlawin, E., Leisenring, J., Misselt, K., et al. 2020, AJ, 160, 231
Segura, A., Kasting, J. F., Meadows, V., et al. 2005, AsBio, 5, 706
Segura, A., Krelove, K., Kasting, J. F., et al. 2003, AsBio, 3, 689
Segura, A., Walkowicz, L. M., Meadows, V., Kasting, J., & Hawley, S. 2010, AsBio, 10, 751
Selsis, F., Wordsworth, R. D., & Forget, F. 2011, A&A, 532, A1
Sergeev, D. E., Fauchez, T. J., Turbet, M., et al. 2022a, PSJ, 3, 212
Sergeev, D. E., Lewis, N. T., Lambert, F. H., et al. 2022b, PSJ, 3, 214
Serindag, D. B., & Snellen, I. A. G. 2019, ApJL, 871, L7
Showman, A. P., & Polvani, L. M. 2011, ApJ, 738, 71
Snellen, I. A. G., de Kok, R. J., le Poole, R., Brogi, M., & Birkby, J. 2013, ApJ, 764, 182
Teal, D. J., Kempton, E. M. R., Bastelberger, S., Youngblood, A., & Arney, G. 2022, ApJ, 927, 90
Tilley, M. A., Segura, A., Meadows, V., Hawley, S., & Davenport, J. 2019, AsBio, 19, 64
Turbet, M., Fauchez, T. J., Sergeev, D. E., et al. 2022, PSJ, 3, 211
Villanueva, G. L., Smith, M. D., Protopapa, S., Faggi, S., & Mandell, A. M. 2018, JJQSRT, 217, 86
Wilson, D. J., Froning, C., Duvvuri, G., et al. 2021a, Mega-MUSCLES Semi-empirical SED of TRAPPIST-1, v1, Zenodo, doi:10.5281/zenodo.4556130
Wilson, D. J., Froning, C. S., Duvvuri, G. M., et al. 2021b, ApJ, 911, 18
Wolf, E. T. 2017, ApJL, 839, L1
Wunderlich, F., Godolt, M., Grenfell, J. L., et al. 2019, A&A, 624, A49
Yassin Jaziri, A., Charnay, B., Selsis, F., Leconte, J., & Lefèvre, F. 2022, CliPa, 18, 2421
Yates, J. S., Palmer, P. I., Manners, J., et al. 2020, MNRAS, 492, 1691
Youngblood, A., Drake, J., Mason, J., et al. 2019, BAAS, 51, 300